Characterization of Read/Write Head Shield Asperities in Hard Disk Drives

Guilherme Parente Souza

Western Digital Storage Technologies (Thailand) Ltd., Ayutthaya, Thailand
Email: Guilherme.Souza@wdc.com

Abstract

A new way to characterize asperities on metallic surfaces at the nanometer scale is proposed. Asperities are often treated using conventional statistical descriptors such as average and root mean square roughness, which do not provide adequate mechanistic insight into surface defect formation and mitigation. The new rationale revolves around developing a mathematical description of the evolution of the area occupied by asperities at each height slice on a topography image, with direct implications on how asperity instances are tracked and their risk of breakage leading to potential exposure and degradation of the metal surface upon thermo-mechanical stresses during the operation of read/write heads is assessed. The technique was shown to be disruptive by surpassing all other surface quality metrics, such as conventional roughness and static area % asperity at 0.5 nm height, in its ability to statistically differentiate surfaces coming from various manufacturing process iterations tailored to produce different surface conditions in the hard disk drive industry. A theoretical formulation proposing that the static asperity technique is fundamentally insufficient, is presented and validated experimentally.

Keywords

DLC, AFM, Surface Characterization, Thin Film, HDD

1. Introduction

Hard disk drives (HDD) are widely known for their large storage capacities and relative affordability compared to solid state devices and are placed centerstage in the data-driven world. HDD manufacturing involves intricate processes and stringent quality control measures while ensuring reliable performance and high data integrity. The head-media interface, where a slider that carries the read/write

head elements flies several nanometers distant from the media at high speeds, concentrates most failure modes that impact HDD reliability such as thermal asperities, corrosion, and scratched media [1] [2] [3]. Thermal asperities refer more generically to surface obstructions that cause localized contact between head and media and generate heat leading to further surface wear and degradation. Corrosion can take place on either head or media, or on both, often because of exposing the bare metals to air under thermal-mechanical stresses associated with flying the head against the media. Scratched media obviously creates tall ridges that come into contact with the head during drive operation. Head scratches are also common, but whether they will cause failure often depends on whether they pass through critical device components. All these failure mechanisms often initiate upon contact with foreign objects such as dust/contamination, hard and/or embedded particles, but may also be related to intrinsic manufacturing defects such as bumps and rough surfaces.

To improve areal density or write/read performance at the smallest possible bit size on the media, the head/media spacing is further reduced upon applying a controlled, thermally induced deformation of the read/write elements during read and/or write operations [4]. Head and media are coated with an ultra-thin (<2 nm) diamond-like carbon (DLC) film that helps preserve the elements both chemically and mechanically throughout the lifetime of the HDD [5] [6]. Head and media top surfaces are also separated by a thin lubricant layer. The read/write block of a magnetic head is shown in **Figure 1** by Atomic Force
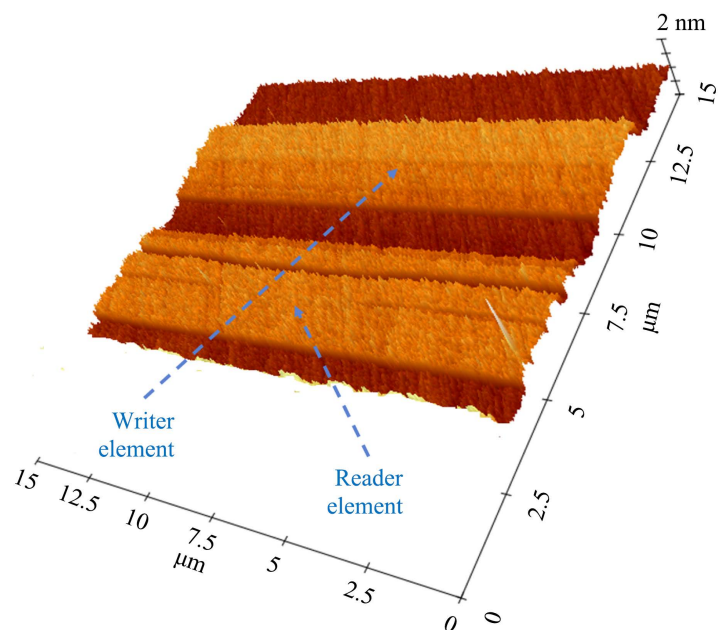

Figure 1. AFM image of the read/write block of a magnetic head, revealing nano-scale roughness on the NiFe shield surfaces. Reader and writer elements are too small to be shown in the image, and only their approximate locations are indicated. The x axis parallel to shields and the y axis perpendicular to shields have um units, whereas the z axis is the z-height of the AFM scan, in nm units.

Microscopy (AFM) topographic image, where it is obvious that surfaces are not atomically flat but instead have various degrees of roughness. The reader sensor stack and the writer pole are less than 50 and 300 nm across, respectively, when looked from a top-down perspective, while most of the read/write block surface is dominated by parallel, rectangular NiFe shields. The shields around the reader are made of electroplated (Ni-rich) $Ni_{80}Fe_{20}$ permalloy with high magnetic permeability and low coercivity to assure the reader sensor detects only the magnetic field from a single bit transition in the disk at a time [7] [8]. The writer pole has a wrap-around structure to help generate a strong and precise magnetic field that effectively alters the magnetic state of the disk's surface during the data writing process. However, the larger portion of the writer block is made of a high magnetic moment (Fe-rich) $Ni_{20}Fe_{80}$ alloy which functions as the return pole for the parallel magnetic recording writer device [9]. Although in the head manufacturing process NiFe surfaces are subjected to lapping, chemical/mechanical cleaning and plasma etching to produce smooth, clean surfaces, the $Ni_{20}Fe_{80}$ shield material is even more prone to localized corrosion, degradation, and surface roughness increase over time due to its higher Fe content compared to the reader shield.

In the context of reader and writer shields, which account for almost the totality of the bearing area in proximity with the disk during read/write operations, shield asperity can be quantitatively defined as the area % of material at a given height slice of an AFM topography scan, which means at least one asperity instance would exist with that specific, minimum height, sticking up from the surface. For example, one can define area % at the 0.5 nm height slice as shield asperity metric, which translates to the relative amount of asperity area equal or higher than 0.5 nm at that surface with respect to the mean topography. In extreme cases where higher asperities are expected, such as when developing lapping and/or plasma etch recipes that define the nano-scale topography at writer and reader elements, for example, higher slices such as 1.0 nm can be utilized to make sure tall asperities are also tracked, taking into consideration they legitimately pose higher quality risk to the magnetic head. Arguably, such view of asperity can only be interpreted in conjunction with established surface topography descriptors [10] such as average roughness (R_a), or the arithmetic mean of the absolute values of the height, and root mean square roughness (R_q), or the mean squared absolute values of the surface roughness profile. R_q is more sensitive to peaks and valleys than R_a due to the squaring of the peak amplitudes. Other common descriptors can also be readily derived from the AFM scan, such as waviness, maximum height, and maximum valley depth, but these as well as the other conventional surface descriptors will not flag the existence of (tall) asperity entities as defined earlier. The focus on area % asperities at a certain height relates to the fact that a tall asperity instance will potentially be in contact with the disk before the rest of the surface, leading to breakage and exposure of the bare metal underneath, thus increasing the risk of subsequent surface degradation, as illustrated in Figure 2. Oxidation of the metal substrate creates localized
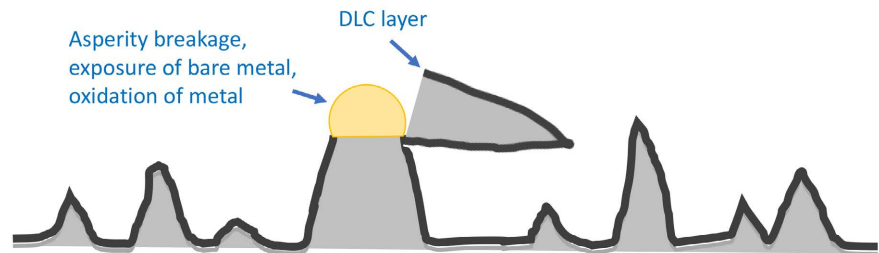
Figure 2. Breakage of tall asperity instances leading to exposure of bare metal, oxidation, and shield degradation.

volume expansion and subsequent, cascading damage to the DLC layer. These effects are amplified by the continuous need to decrease head-to-disk spacing to enable higher capacity drives, which is often achieved by a combination of thinner DLC layers and lower flight heights that dramatically increase the risk of contact. Thinner DLC means less coverage of ridges formed by tall asperities, as well as overall higher risk of oxygen diffusion into the Fe-rich alloy even without film breach [11]. Tall asperities also have a higher tendency to pick up lubricant and contamination, potentially increasing the flight height and decreasing HDD performance. New HDD technologies designed to increase areal densities and storage capacities per platter, such as heat-assisted magnetic recording (HAMR) [12], may impose even more stringent requirements with respect to surface flatness and shield asperities, and as a result the asperity problem will continue to be relevant in the future of the HDD industry. In the present study, the conventional understanding of shield asperity characterization is revisited and confronted with a novel, potentially disruptive rationale.

2. Materials and Methods

The samples used in this study are actual magnetic heads that underwent a variety of different process steps to intentionally produce various NiFe surface conditions in terms of asperities. It is important to disclose that the intent is to produce different surface conditions to evaluate different asperity characterization methods. Detailed information of process parameters is out of the scope of the presence study, and instead only a high-level guide of the implications of each different process on the surface condition is listed below and discussed throughout the text where applicable.

The final processes that define the surface condition of a magnetic head with respect to roughness and asperities are chemical/mechanical cleaning (post lapping), ion-beam etch (IBE), and subsequent DLC film deposition. The DLC is produced via the filtered cathodic arc (FCA) process [9]. The samples used in this study can be grouped as follows:

- DLC thickness: DLC1 < DLC2 < DLC3; DLC4 is a thinner film with different carbon properties not related to the others.
- IBE: This process is intended to remove native oxides from the prior lapping and cleaning step. IBE2 uses Ar-O plasma and is expected to produce rough-

er NiFe surfaces compared IBE1.

- CLEANING: This group has four sub-groups permutating between two different post-lapping/cleaning processes and two target removals of oxide layer *i.e.* REM High/CL2, REM Low/CL1, REM Low/CL2, and REM High/CL1.
- VOLTAGE: This group has three sub-groups with different IBE voltage levels *i.e.* IBE-V High, IBE-V Low, and IBE-V Med. This group is different from the IBE group above, since only the voltage itself is varied, whereas the IBE group uses a combination of incidence beam angle, etch time and voltage to deliver widely different surface conditions.

All the experimental data in this study consists of AFM scans on the NiFe writer shield that includes the writer pole. The data was acquired using a Park Systems XE series AFM tool in non-contact mode. The scan size was 1.0 μm × 1.0 μm, with a down-track resolution of 2048 pixels. The AFM scans are levelled using well known procedures. All subsequent data analysis, shown in this manuscript, derive solely from the acquired/leveled data matrix from the AFM. A custom-made Python script was coded by the author to automatically produce the height slice analysis and modeling, which will be described in detail on the next section, as well as conventional roughness analysis. Here, the concept of a height slice consists of all the material present at and above a given height on the topography derived from an AFM scan. For example, a 0.7 nm asperity instance would be visible at the 0.5 nm height slice but would not be visible at the 1.0 nm height slice. The area % occupied by that material at that height slice can be measured, for example. Mathematical simulations were also implemented in Python. Asperities and roughness results were consolidated comparatively using SAS JMP software.

3. Results

3.1. Shield Asperities Characterization Methods Compared

The area % asperities approach at a fixed height slide is illustrated in **Figure 3**. The standard AFM topography scan of the writer pole and surrounding writer shield is shown in **Figure 3(a)**, where the brighter the appearance the taller the corresponding surface feature with respect to the mean surface. **Figure 3(b)** is the 0.5 nm height slice, where in yellow are only the asperities equal or higher than 0.5 nm. The area % of asperities corresponding to this height slice is ~3.1% and, based on the fixed area % definition, this is the metric that will differentiate between a "good" and a "bad" surface with respect to asperities *i.e.* the higher the area % value at a fixed height slice the worse the surface. **Figure 4(a)** shows, for the same writer shield shown in **Figure 3**, a few additional height slices representing the full stack of height slices up to 0.5 nm, plus the 1.0 nm slice for comparison, which is a more dynamical picture of the area % asperity evolution with height slice. In this case there was significant decrease in asperities area % between 0.2 nm and 0.4 nm, and only two or three very thin asperity instances are higher than 1.0 nm, barely detectable. These taller asperities are much higher
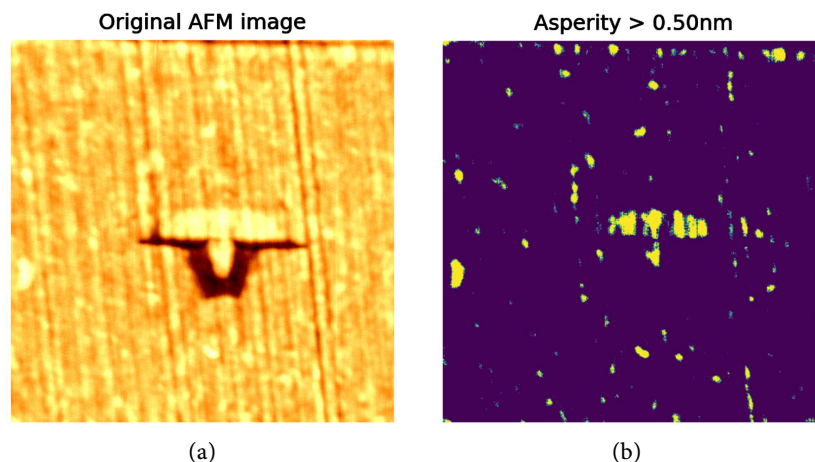
Original AFM image | Asperity > 0.50nm

(a)   (b)

Figure 3. (a) Original AFM topography image. (b) For the same AFM scan, the area % of asperities at the 0.5 nm height slice (~3.1%). Image size is 1.0 μm × 1.0 μm.

than the V-shaped writer pole device, which also stands out from the surface. Other surface features such as lapping scratches decreased rapidly within the first height slices and are no longer visible at the 0.5 nm slice. The complete evolution of the area % asperities with discrete height slice steps of 0.02 nm is shown on the plot in **Figure 4(b)**, confirming the semi-quantitative inferences made for **Figure 4(a)** and providing a much more thorough description of the surface. The asperity decay with height slice plot can be modeled with a logistic decay fit [13] of the form (Equation (1)):

$$f(x) = \frac{c}{1 + ae^{-bx}} \tag{1}$$

In Equation (1), a ($a > 0$), b ($b < 0$ is the decay rate) and c ($c > 0$) are fitting parameters that will be explored throughout this study. The model is derived from the Verhulst-Pearl equation of population growth over time (when $b > 0$), except in this case it refers to a decay with parameter b assuming negative values, and the decaying population is that of asperities at a given height slice x. As the model describes processes that exhibit initial rapid decay followed by a slower decline until reaching a stable minimum value, the first approach was to use the decay rate b to parameterize the risk of asperity breakage *i.e.* the faster the asperities transition from a high area % (strong bearing area) to only a few instances sticking up against the disk, as the HDD operates, the less robust is the NiFe shield with respect to asperities. Other permutations using a, b and c were evaluated. One of them was related to the initial bearing area at $x = 0$ *i.e.* $c/(1 + a)$. Since c does not carry any significant meaning for decay curves (for growth curves this is called *carrying capacity i.e.* the function approaches c as x goes to infinity), the logical path is to combine only the denominator $(1 + a)$ with b as a multiplying factor *i.e.* $b(1 + a)$.

The asperity area % at a given height slice is static and deliberate (**Figure 3(b)**). The new rational attempts to provide a dynamical view of asperity, starting from the tallest asperity instances first in contact with the disk and ending at
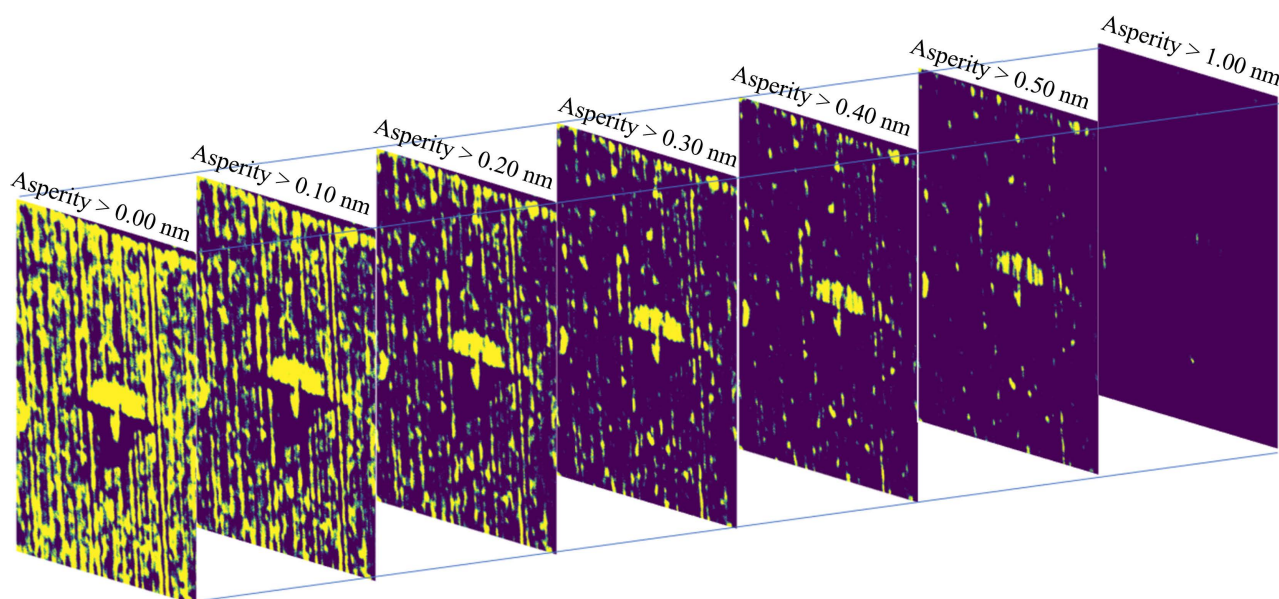
(a)
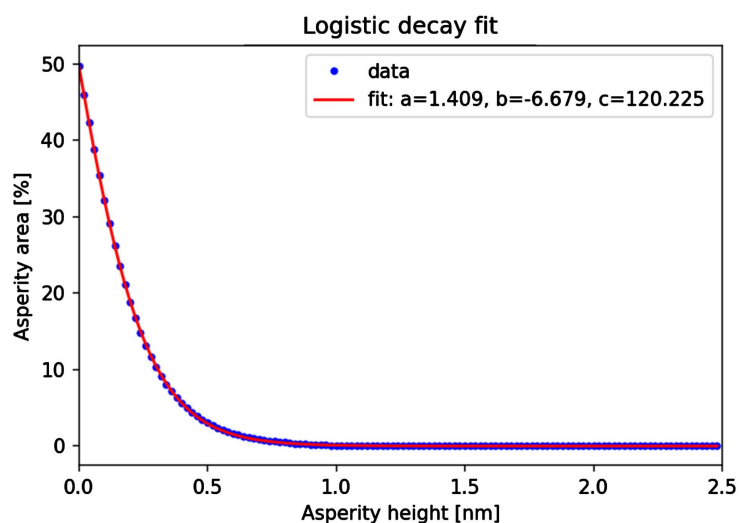
(b)

Figure 4. (a) A few discrete height slices for the same AFM scan of **Figure 3**. (b) Evolution of the area % asperities as a function height slice with 0.02 nm step. The curve was fitted with a logistic decay model.

the NiFe surface roughness and waviness including scratch marks (**Figure 4**). Using experimental values for *a, b* and *c* in Equation (1) after fitting the logistic decay model for all samples utilized in this study, as well as the grand mean of area % at 0.5 nm height representative of all samples equal to ~4.6%, it is possible to simulate infinite surfaces that pass through the $x = 0.5$ nm, $y = 4.6$ area % point. This analysis, shown in **Figure 5(a)** and **Figure 5(b)**, suggests that the static asperity definition is fundamentally insufficient to describe the nature of surface asperities and its relation to quality risk, since any static measurement of asperities (*i.e.* fixed slice height) can represent a multitude of surfaces with various risk levels based on either *b* or *b*(*a* + 1). To illustrate this analysis, the slices
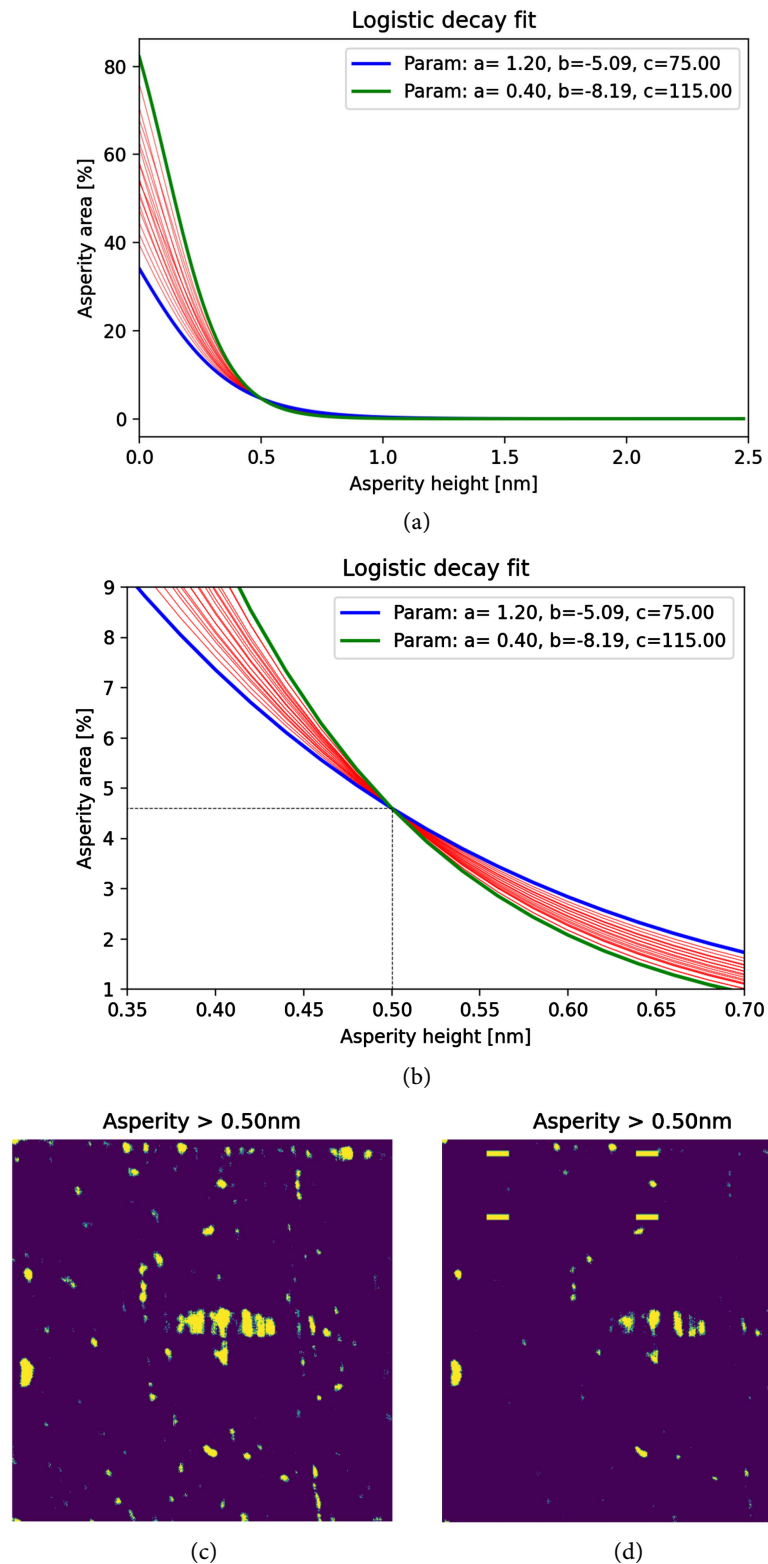
(a)

(b)

(c)

(d)

Figure 5. (a) Simulation of infinite surfaces that pass through the x = 0.5 nm, y = 4.6 area % point based on the logistic decay model. (b) Same curve zoomed in. (c) and (d) have the same area % asperities at the 0.5 nm (~3.1%), but (c) had the overall asperities artificially decreased and six rectangular asperity instances were added to the top part of the NiFe. Image size is 1.0 μm × 1.0 μm.

shown in **Figure 5(c)** and **Figure 5(d)** have the same area % asperities at the 0.5 nm (~3.1%), but the one on **Figure 5(d)** had the overall asperities artificially decreased by an arbitrary factor and subsequently six rectangular (for simplicity) asperity instances were added to the top part of the NiFe. Based on the static asperity definition, those two surfaces would have the same quality risk, although the one on **Figure 5(d)** is clearly more prone to damage upon contact with the disk than the one on **Figure 5(c)** due to the tall asperity instances (artificially) added to the surface. As the overall shield topography analysis would also take into consideration roughness (R_a and R_q), the surface shown in **Figure 5(c)** would be considered flatter compared to the one on **Figure 5(d)**, further compromising the risk assessment correctness.

3.2. Applying Different Rationales Comparatively on Different NiFe Surfaces

R_a and R_q roughness metrics for all samples utilized in this study are shown in **Figure 6(a)** and **Figure 6(b)**. Student's statistical parameter was used to quantify the extent of statistically meaningful separation between the sample groups with respect to roughness. The more separated the circles the more statistically distinguishable are the groups from one another. DLC2 and IBE1 have distinctively lower asperity levels. DLC4 and IBE2 have higher roughness levels, but the differences are not so significant. There are inconsistencies between R_a and R_q, the most significant being for the CLEANING group which has higher roughness with respect to R_q but lower roughness with respect to R_a. The roughness analysis is somewhat insufficient to clearly differentiate sample groups that are expected to show clear differences, which leads to the reasoning that the asperity analysis is critical to understanding surface conditions. **Figure 7** shows the comparison between the static asperity definition and the dynamical rationale, here represented by both the fitting parameter b and the combined $b(1 + a)$. It is important to note that the asperity area % at the 0.5 nm height slice brings better differentiation between the groups compared to R_a and R_q, also addressing the distinctiveness of the CLEANING group, for example, which was poorly defined from the roughness perspective alone (**Figure 6**). However, the static asperity definition does not distinguish the various sample groups as effectively as either b or $b(a + 1)$ from the logistic decay fit. The b parameter does not perform so well for the first group on the left of **Figure 7(b)**, but clearly shows less variability among samples of a same group. This improvement is even better for $b(1 + a)$ in **Figure 7(c)**, where the parameterization resolves differences between groups even more evidently. This result suggests that the curve fitting approach is less sensitive to localized variations between samples within the same group representing any given surface or manufacturing process, thus capturing the true, representative features of each surface group. The data also reveals that the DLC thickness has a smaller effect to the NiFe surfaces studied, with the DLC2 group standing out with less asperities and/or risk associated with asperities. This result suggests that the DLC3 group, although having a thicker DLC film, may

have undergone unintentionally a more aggressive plasma etch exposure, here assigned to natural process variation. IBE1 and IBE2 groups are the most statistically separated pairwise, which is expected since different etch recipes can strongly change the metal surface [14]. It is postulated that non-uniform oxidation of the original surface prior to IBE leads to preferential etching of those more oxidized spots, exacerbating the non-uniformity and surface roughness (and asperities). Here it is important to note that both oxidation and etching creates a magnetically dead layer either by damaging the atomic (NiFe) lattice or by replacing it with oxides, or both. At the nano-meter scale, the altered surface will have lower density than the bulk.
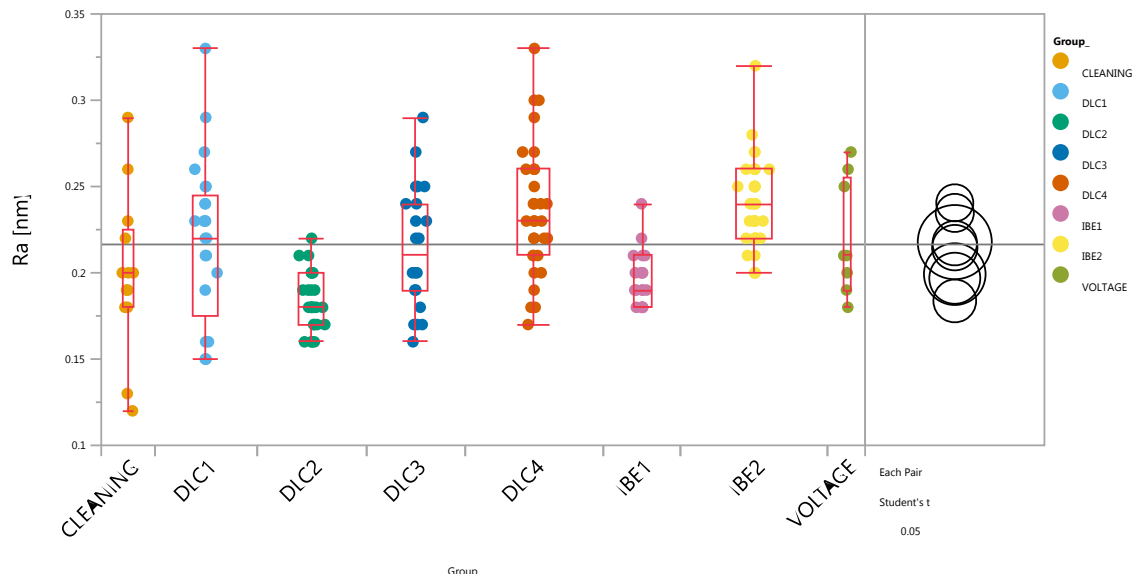
(a)
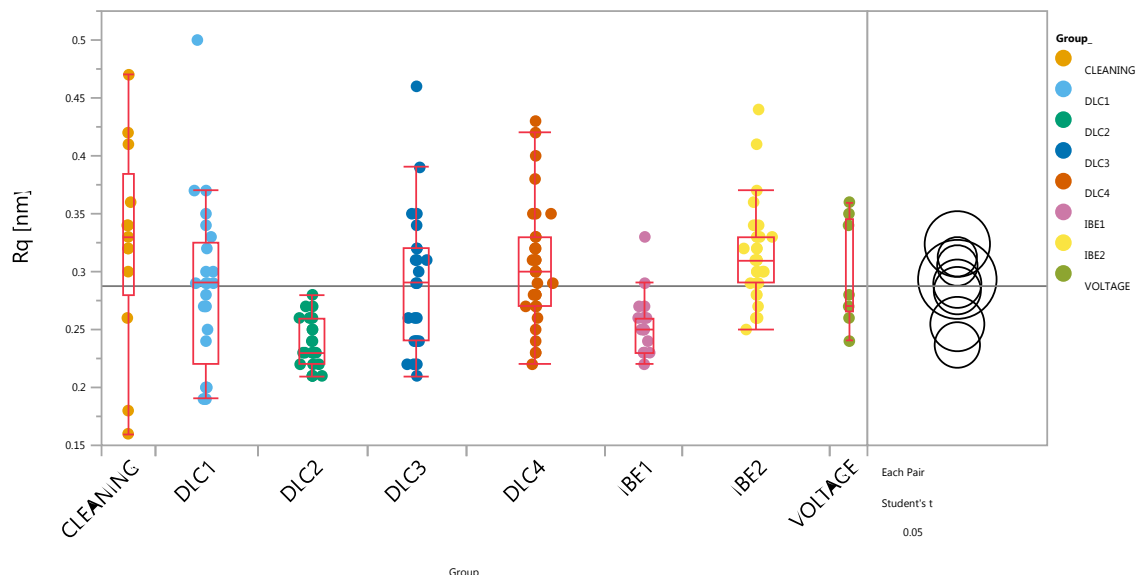
(b)

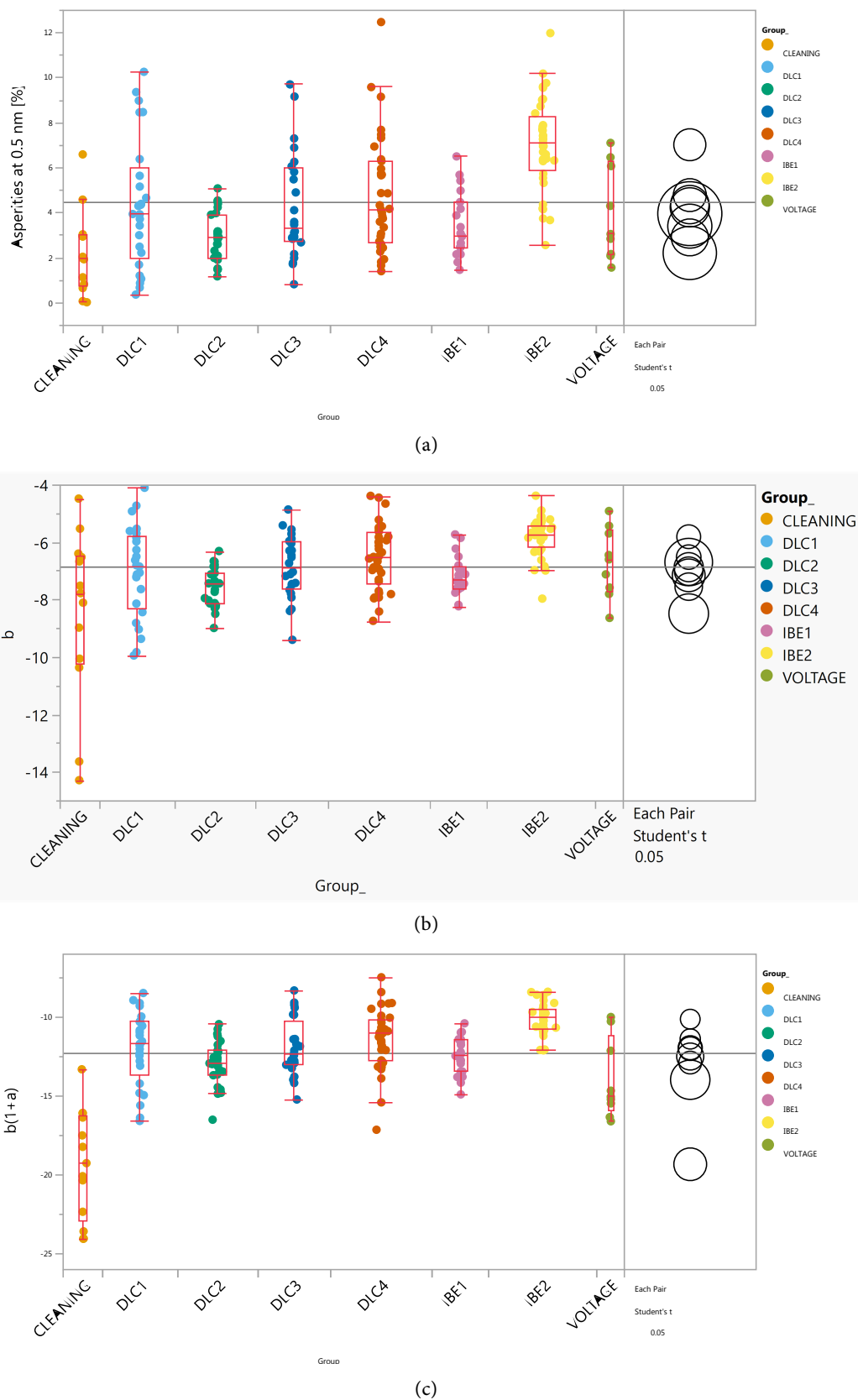**Figure 6.** (a) R_a and (b) R_q roughness measurements for all samples.

Figure 7. Asperity metrics compared: (a) static metric area % at the 0.5 nm height slice, (b) dynamical metric using the b parameter from the logistic decay fit, and (c) $b(a+1)$.

The CLEANING and VOLTAGE groups have a higher variability. Sub-groups within these groups are examined in detail in **Figure 8(a)** using the static asperity definition and in **Figure 8(b)** using the parameterization $b(a + 1)$. The low IBE voltage samples have evidently poorer surfaces compared to mid and high voltage samples. The new rational resolves these groups more effectively compared with the conventional definition. Using $b(a + 1)$, it is possible to, at least marginally, suggest that the high voltage sub-group has the best NiFe surface. This further validates the usefulness of the new rationale in designing IBE recipes
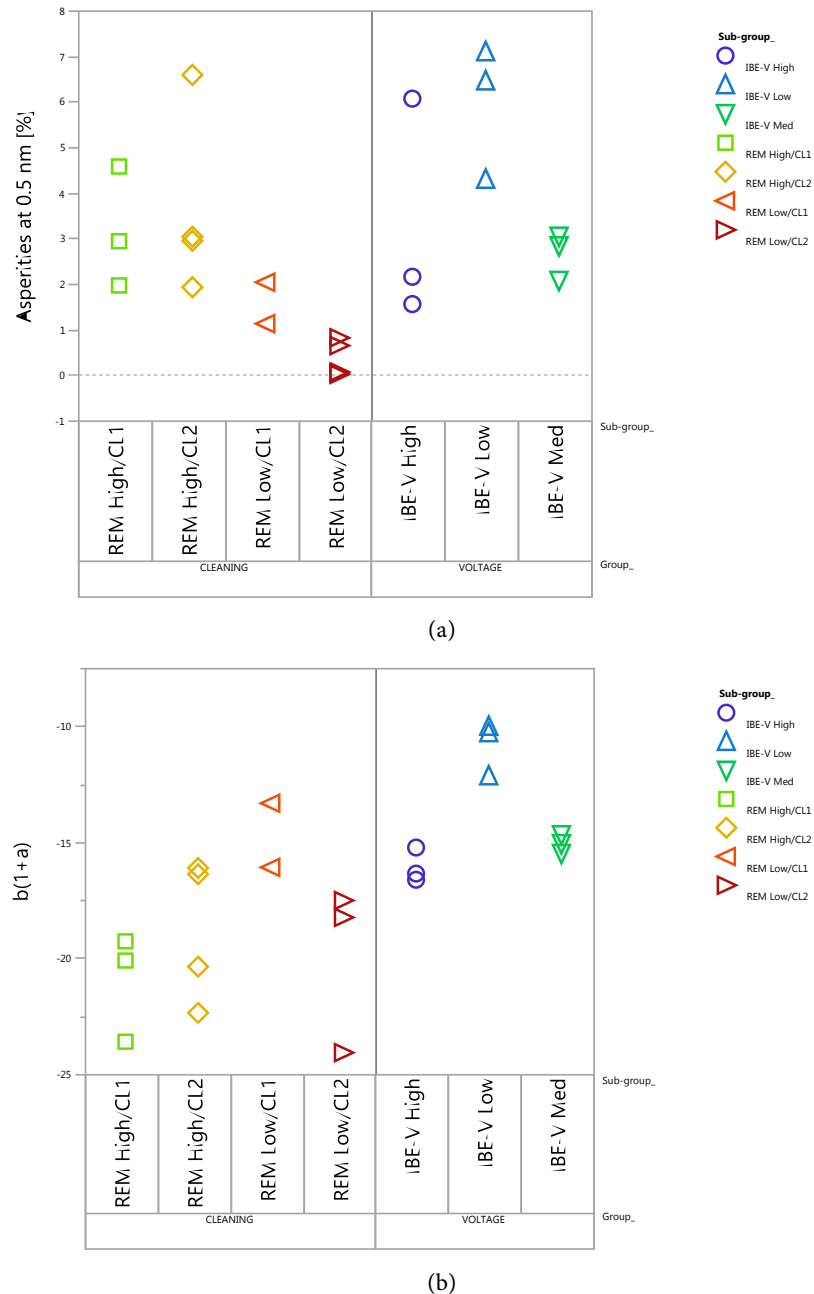

(a)

(b)

Figure 8. Sub-groups within the CLEANING and VOLTAGE groups are examined in detail using (a) the static asperity definition and (b) the parameterization $b(a + 1)$.

for HDD applications. The CLEANING group has a more complex framework with a mix of cleaning processes and oxide removal targets. In terms of oxide removal, the new asperity rational places the two high removal sub-groups REM High/CL1 and REM High/CL2 at the lower bottom of $b(a + 1)$, which is consistent with the goal of removing more of the oxide layer to create a flatter and more uniform surface. This is also in line with the observations made for the low vs. mid vs. high voltage sub-groups. In terms of different cleaning processes, none of the metrics seems to be a suitable differentiator, which suggests that the cleaning processes evaluated do not pose, comparatively, radically different risks.

The results confirm that the new asperity rationale brings new light on the surface quality assessment, as well as can resolve differences between various groups and/or sub-groups of samples, highlighting differences among various manufacturing processes. By plotting the new rationale vs. static asperity definition (Figure 9), it is clear that at a high level the two definitions are correlated *i.e.* the higher the area % at the 0.5 nm height slice the higher $b(1 + a)$. The correlation is reasonably linear above the 2 - 3 area % asperities, with a stronger curvature as the asperity levels approach zero. However, when viewed in terms of the risk posed by a tall asperity instance, such as in the case highlighted with a red circle and its corresponding AFM image with a white dot near the center (a very tall, solitary asperity instance), compared with a relatively good surface circled in green, one can observe that both surfaces are considered to be "low asperity risk" using the static definition, whereas with the new rationale there is a clear separation between good vs. bad surfaces. The other outliers to the correlation mostly follow the same logic *i.e.* the new rationale can detect representative characteristics that affect asperity breakage risk. This experimental fact validates the theoretical approach presented in Figure 5.
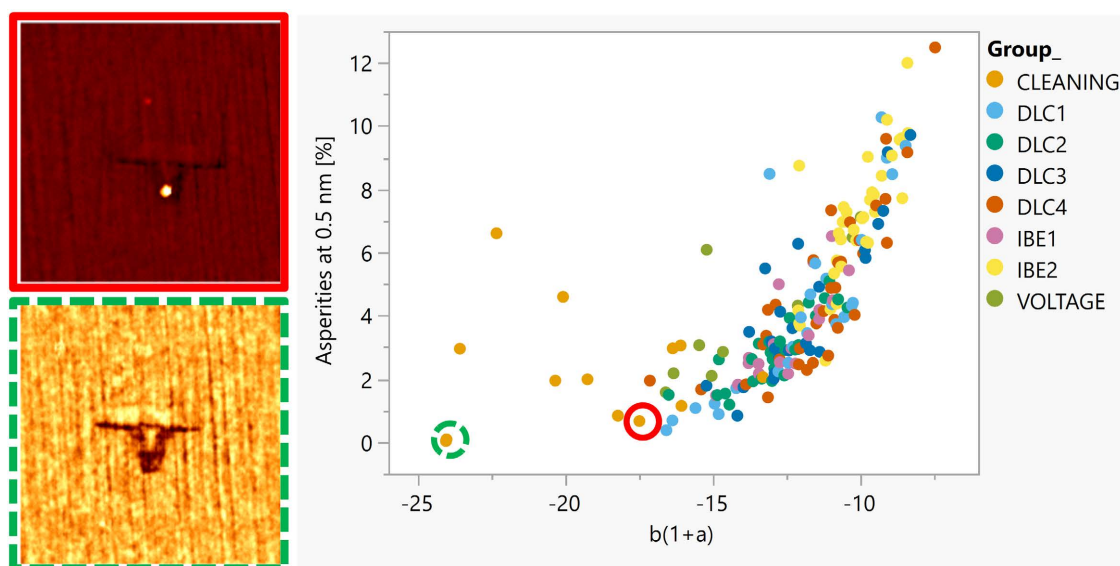

Figure 9. New $b(1 + a)$ vs. static area % at the 0.5 nm slice height asperity definition plot. AFM topography images for selected samples on the plot are shown on the left. Image size is 1.0 um × 1.0 um.

4. Discussion

The area under the area % asperities curve fitted with the logistic decay function should yield the vol % asperities. Using that mathematical intuition and an integration interval of 0 - 2 nm height (and not 0 - 1 nm) to compensate for the fact that only asperities above the mean contribute to the area % plot, it is possible to obtain the approximate vol % asperities per nanometer (height). The integration interval also covers a reasonably broad range of slices even for unreasonably tall asperities, thus preventing information suppression. **Figure 10** shows a plot of vol % asperities for all samples analyzed in the present study. Expectedly, since the metric derives from area %, the results show the same trend as in **Figure 7**. One potential differentiator between vol % asperities and $b(a + 1)$ is that, in principle, vol % does not care about how fast any given asperity instance would disappear with increasing height slice, but only about the totality of volume (space) occupied by asperities, including short, tall, and even scratch marks, which could be useful for some applications such as flatness assessment and monitoring for the lapping process.

Another parameter that can be extracted from each height slice is the number of asperities. In the present work, the computational implementation utilized was a Blob Detector algorithm based on The Laplacian of Gaussian formulation [15]. Essentially, the algorithm detects regions in the (AFM height slice) image that differ in color in this case yellow vs. dark blue, compared to surrounding regions. The evolution of the number of asperities with discrete height steps of 0.02 nm is shown in **Figure 11(a)**. Number of asperities can be described using a more complex, five-parameter logistic model [16] of the asymmetrical sigmoidal form (Equation (2)):
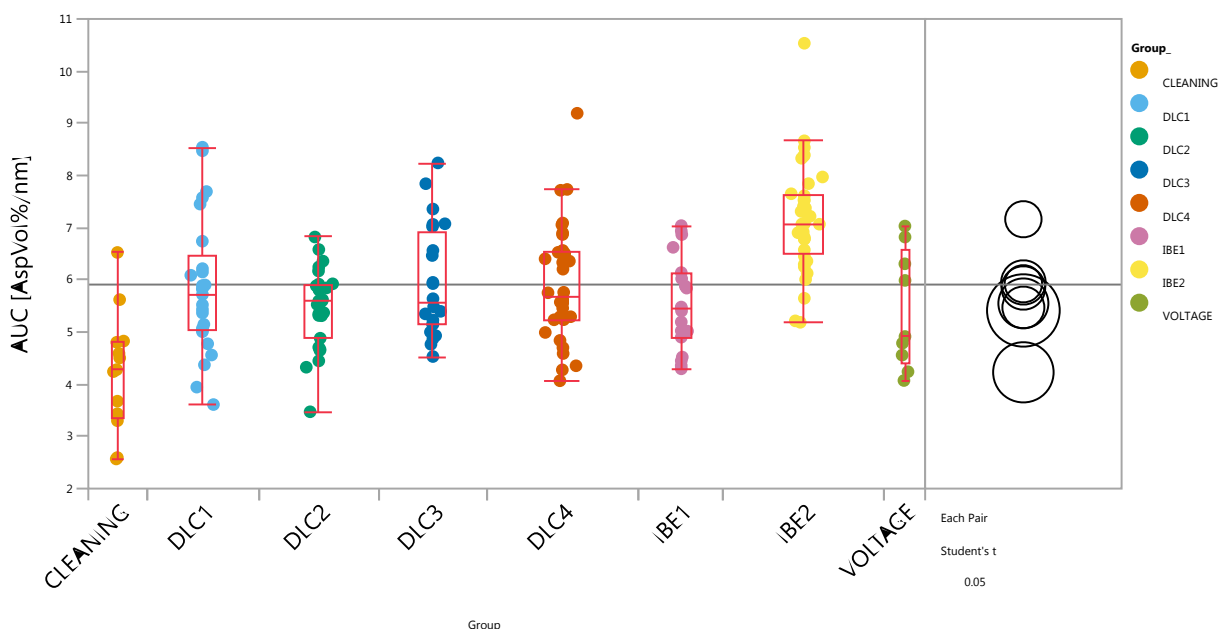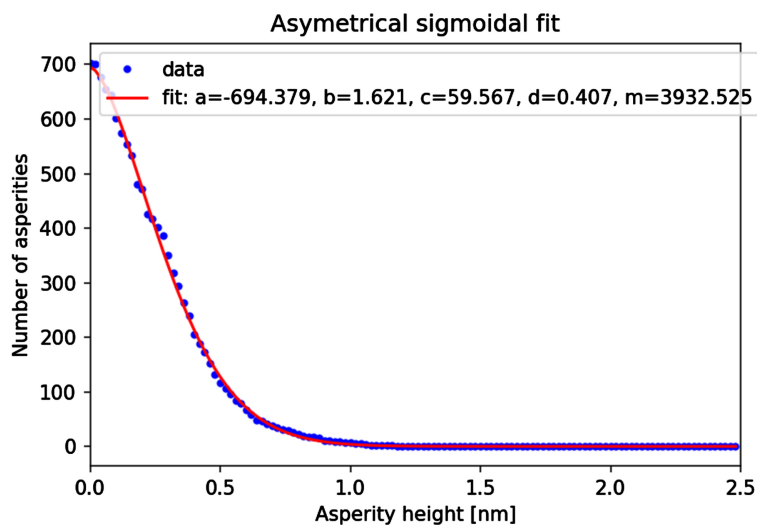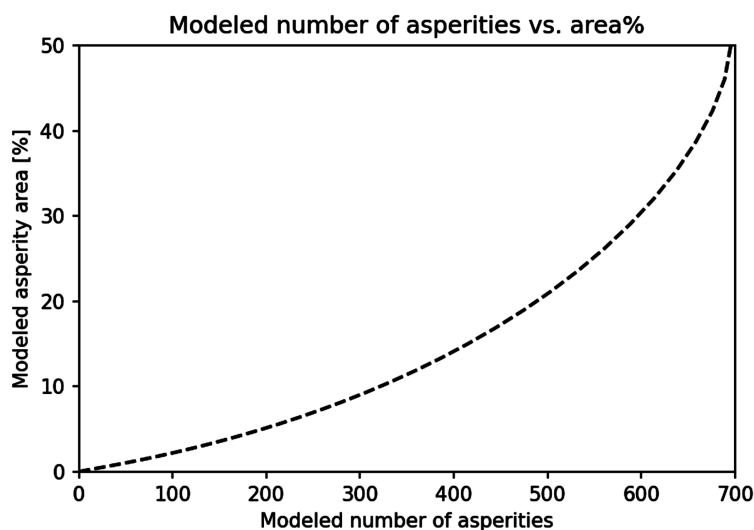

Figure 10. Comparative plot of the vol % asperities for all samples.

(a)

(b)

Figure 11. (a) Evolution of the number of asperities as a function height slice with 0.02 nm step. The curve was modeled with an asymmetrical sigmoidal fit. (b) Modeled number of asperities using the asymmetrical sigmoidal fit vs. the modeled area% using the logistic decay fit.

$$f(x) = d - \frac{a - d}{\left(1 + (x/c)^b\right)^m} \qquad (2)$$

In Equation (2), $2d - a$ is the number of asperities at the zeroth height slice, b is the steepness of the curve, c is the inflection point, and m is the asymmetry factor. This fit was chosen since it can accommodate the fact that at the first few height slices the number of asperities tends to be largely unchanged until the shortest asperities (which comprise surface roughness) start to disappear. This effect is evidenced by the plot of modeled number of asperities using the asymmetrical sigmoidal fit vs. the modeled area % using the logistic decay fit, shown

in **Figure 11(b)**, where it becomes evident that the number of asperities drops slower than area % near the mean plane (right-hand side of the plot), but as only a few, tall asperity instances populate the (tallest) height slices, those asperities will undergo rapid decrease in area % (*i.e.* equivalent diameter) while the numbers will remain relatively unchanged (left-hand side of the plot). An interesting insight that can be drawn from this result is that the average asperity diameter can be calculated by dividing the area % by the number of asperities *i.e.* the average diameter of each asperity instance at each height slice. With that, one can estimate the average aspect-ratio (*i.e.* height/diameter) for the asperity instances at each height slice, which could potentially offer an even more realistic picture of the risk of the asperities to fracture and expose the bare metal underneath. Such a plot of average aspect ratio vs. height slice is shown in **Figure 12**. For this sample, which is the one shown in **Figures 3-5**, the aspect ratio calculation breaks down as it approaches the ~1.3 nm height slice and the algorithm can no longer track asperity instances effectively. The discontinuity shown at the ~0.9 nm height slice corresponds to a discrete transition into just two (possibly three) asperity instances with marginally small diameter. These asperities correspond to the highest risk entities within that area of the NiFe shield where the AFM scan was performed, believed to be representative of the rest of the bearing surface. It is possible to add intelligence to the algorithm to track, for example, the evolution of the one or two highest asperity entities throughout the entire height profile. This would be, in many ways, equivalent to the average aspect ratio profile, but just more accurate and would not change the assessment of severity level of surface spikes. A compromise could be made between scan speed, matrix size and resolution to detect more asperity instances at the risk of blurring their aspect ratio. As part of a quality inspection, failure analysis, and/or process development scheme, it is crucial to define and maintain those key data acquisition parameters.
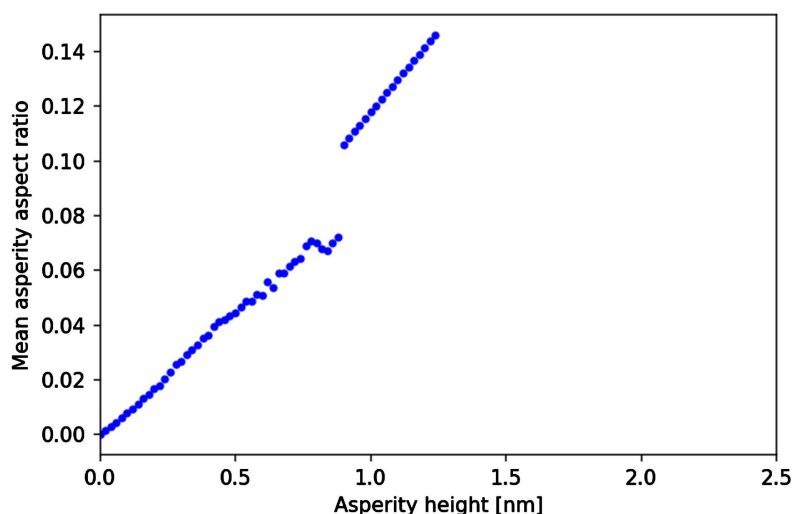

Figure 12. Estimate of the average aspect-ratio for the asperity instances present at each height slice.

A final consideration for the height slice modeling technique is whether this could benefit other types of surfaces, such as media (disk) in the HDD industry, as well as outside. First and foremost, the same concern about the presence and risk level of (tall) asperities on a magnetic head can be directly translated to media, since at the end the head will fly over the media at very close proximity. The only requirement for media asperity quantification is to set up appropriate acquisition parameters to cover the most possible disk area at the shortest possible time, and to apply the rationale including evaluating whether the same parameterization would be adequate (*i.e.* $b(a + 1)$) or not. The disk surface is infinitely larger than that of the head or the NiFe shield surface, and thus an appropriate sampling scheme needs to be developed for media. The same could be said to other industries such as automotive and aerospace including metalworking and machining, where surface friction is a crucial aspect of the quality and performance of parts and of integrated systems. The optics industry, including optical components, lenses, mirrors, and precision instruments rely on asperity quantification to maintain high-quality surfaces, minimize scattering, and improve optical performance. Orthopedic implants in the medical sector where biological and inorganic surfaces will interact could be a potential candidate as well. In the consumer electronics sector, smartphones and tablets rely on high-quality surfaces that translate touch sensitivity and enhance user experience. Moreover, the type of fitting model, whether it will be a three-, four- or five-parameter logistic model, depends on the characteristics of the surface, although I would expect the methodology itself to be disruptive in the sense that it will provide additional insight into manufacturing processes and failure modes related to engineered surfaces compared to more conventional roughness metrics.

5. Conclusion

This work compares conventional surface roughness metrics such as R_a and R_q with asperity metrics by evaluating metal shields that fly in close proximity of the rotating media disks. The static asperity definition based on area % of material higher than a height threshold or slice was shown to resolve differences between sample groups somewhat better than conventional roughness metrics. A new rationale, in which the entire range of height slices from the mean surface to the tallest asperity instances is described mathematically, offers a more dynamical view of the surface condition in terms of the risk posed by a few, tall asperity instances to function as the bearing area on head-disk contact. The new idea was capable to differentiate various types of NiFe surfaces coming from a range of manufacturing processes adjustments, in a way that surpasses all the other surface descriptors analyzed. The experimental results validated a theoretical approach, which was also proposed in this study. The area % asperity as a function of height slice was modeled with a three-parameter logistic function. The parameterization $b(a + 1)$ was the most promising in terms of capturing process representative features and distinguishing sample groups more effec-

tively. A vol % asperities model was also defined. In terms of sample group differentiation, the ion-beam etch process was expectedly shown to promote the highest surface change, and the cleaning process the least change with respect to asperities. The number of asperities for each height slice was calculated using a computer vision algorithm and required a more complex, five-parameter model to fit the experimental data. With area % and number of asperities, a path was established to estimate and track the average asperity diameter and aspect-ratio for each height slice.

Acknowledgements

Author Contributions

Original idea, conceptualization and writing, original draft preparation, G.P.S.; the author has read and agreed to the published version of the manuscript.

Conflicts of Interest

The author declares no conflict of interest.

References

[1] Elerath, J.G. and Pecht, M. (2007) Enhanced Reliability Modeling of RAID Storage Systems. *37th Annual IEEE/IFIP International Conference on Dependable Systems and Networks* (*DSN*'07), Edinburgh, 25-28 June 2007, 175-184. https://doi.org/10.1109/DSN.2007.41

[2] Strom, B.D., Lee, S.C., Tyndall, G.W. and Khurshudov, A. (2006) Hard Disk Drive Reliability Modeling and Failure Prediction. *Asia*-Pacific Magnetic Recording Conference 2006, Singapore, 29 November-1 December, 2006, 1-2. https://doi.org/10.1109/APMRC.2006.365900

[3] Khurshudov, A. and Ivett, P. (2003) Head-Disk Contact Detection in the Hard-Disk Drives. *Wear*, **255**, 1314-1322. https://doi.org/10.1016/S0043-1648(03)00201-1

[4] Juang, J.Y. and Bogy, D.B. (2007) Air-Bearing Effects on Actuated Thermal Pole-Tip Protrusion for Hard Disk Drives. *Journal of Tribology*, **129**, 570-578. https://doi.org/10.1115/1.2736456

[5] Souza, G.P., Ruthe, K.C., Chen, L., Hong, L. and Wang, H. (2015) Materials Selection for Ultra-Thin Diamond-Like Carbon Film Metrology and Structural Characterization by TEM. *Microscopy and Microanalysis*, **21**, 827-828. https://doi.org/10.1017/S1431927615004936

[6] Puttichaem, C., Souza, G.P., Ruthe, K.C. and Chainok, K. (2021) Characterization of Ultra-Thin Diamond-Like Carbon Films by SEM/EDX. *Coatings*, **11**, 729. https://doi.org/10.3390/coatings11060729

[7] McFadyen, I.R., Fullerton, E.E. and Carey, M.J. (2006) State-of-the-Art Magnetic Hard Disk Drives. *MRS Bulletin*, **31**, 379-383. https://doi.org/10.1557/mrs2006.97

[8] Tuggle, A., Gider, S., Mauri, D. and Ho, M. (2013) Shield Design for Enhanced Read-

er Resolution. *IEEE Transactions on Magnetics*, **49**, 3729-3732. https://doi.org/10.1109/TMAG.2013.2246783

[9] Osaka, T. (1999) Recent Development of Magnetic Recording Head Core Materials by Plating Method. *Electrochimica Acta*, **44**, 3885-3890. https://doi.org/10.1016/S0013-4686(99)00095-X

[10] De Oliveira, R.R.L., Albuquerque, D.A.C., Cruz, T.G.S., Yamaji, F.M. and Leite, F.L. (2012) Measurement of the Nanoscale Roughness by Atomic Force Microscopy: Basic Principles and Applications. In: Bellitto, V., Ed., *Atomic Force Microscopy—Imaging, Measuring and Manipulating Surfaces at the Atomic Scale*, In-Tech, Rijeka, 147-174. https://doi.org/10.5772/37583

[11] Souza, G.P., Ruthe, K.C. and Leary, S.P. (2018) Si Diffusion in Ultra-Thin Tetrahedral Amorphous Diamond-Like Carbon. *Proceedings of the* 19*th International Microscopy Congress* (*IMC* 19), Sydney, 9-14 September 2018, 1345.

[12] Kiely, J., Jones, P. and Hoehn, J. (2018) Materials Challenges for the Heat-Assisted Magnetic Recording Head-Disk Interface. *MRS Bulletin*, **43**, 119-124. https://doi.org/10.1557/mrs.2018.4

[13] Tsoularis, A. (2001) Analysis of Logistic Growth Models. *Research Letters in the Information and Mathematical Sciences*, **2**, 23-46.

[14] Si, W., Williams, K., Campo, M., Mao, M., Devasahayam, A. and Lee, C.L. (2005) Determination and Reduction of Ion-Beam Etching Induced Magnetic Dead Layer. *Journal of Applied Physics*, **97**, 1-3. https://doi.org/10.1063/1.1851871

[15] Lindeberg, T. (2015) Image Matching Using Generalized Scale-Space Interest Points. *Journal of Mathematical Imaging and Vision*, **52**, 3-36. https://doi.org/10.1007/s10851-014-0541-0

[16] Gottschalk, P.G. and Dunn, J.R. (2005) The Five-Parameter Logistic: A Characterization and Comparison with the Four-Parameter Logistic. *Analytical Biochemistry*, **343**, 54-65. https://doi.org/10.1016/j.ab.2005.04.035